2017

Time-Varying and Constant Switching Frequency-Based Sliding-Mode Control Methods for Transformerless DVR Employing Half-Bridge VSI

Hasan Komurcugil

Samet Biricik

Time-Varying and Constant Switching Frequency-Based Sliding-Mode Control Methods for Transformerless DVR Employing Half-Bridge VSI

Hasan Komurcugil, *Senior Member, IEEE*, and Samet Biricik, *Member, IEEE*

***Abstract*—This paper presents time-varying and constant switching frequency based sliding-mode control (SMC) methods for three-phase transformerless dynamic voltage restorers (TDVRs) which employ half-bridge voltage source inverter. An equation is derived for the time-varying switching frequency. However, since the time-varying switching frequency is not desired in practice, a smoothing operation is applied to the sliding surface function within a narrow boundary layer with the aim of eliminating the chattering effect and achieving a constant switching frequency operation. The control signal obtained from the smoothing operation is compared with a triangular carrier signal to produce the pulse width modulation signals. The feasibility of both SMC methods has been validated by experimental results obtained from a TDVR operating under highly distorted grid voltages and voltage sags. The results obtained from both methods show excellent performance in terms of dynamic response and low total harmonic distortion (THD) in the load voltage. However, the constant switching frequency-based SMC method not only offers a constant switching frequency at all times and preserves the inherent advantages of the SMC, but also leads to smaller THD in the load voltage than that of time-varying switching frequency-based SMC method.**

***Index Terms*—Constant switching frequency, dynamic voltage restorer (DVR), sliding-mode control (SMC), time-varying switching frequency.**

I. Introduction

DYNAMİC voltage restorers (DVRs) are custom power devices used to protect sensitive loads from the voltage sags, swells, and harmonics existing in the electrical grid at the point of common coupling (PCC) [1], [2]. Generally, the DVR circuit consists of a dc voltage source, a voltage source inverter (VSI) together with an *LC* filter and a series transformer [3]. The load protection is achieved successfully if the DVR injects a desired compensating voltage through the series transformer into the grid such that the load voltage is unaffected from the undesired voltage variations at PCC. In order to inject the desired compensating voltage, the DVR should be operated by using a proper control strategy, which offers a fast transient response, possesses strong robustness to parameter variations, and requires less complexity in a practical implementation.

The requirements mentioned above have been fulfilled by various control strategies proposed for conventional DVRs [4]–[20]. They are based on feedback control [4], [5], H-infinity control [6], fuzzy logic control [7], repetitive control [8], hysteresis control with constant switching frequency [9], different voltage injection methods developed in the synchronous reference frame [10], and sliding-mode control [11]–[15]. The design of capacitor-supported DVR topologies are also investigated [16]–[18]. The interline DVR presented in [19] consists of several DVRs and shares a common dc link connecting independent feeders. In [20] and [21], the DVR is realized by employing a multilevel inverter.

The aforementioned DVR topologies and control strategies yield various advantages and disadvantages related to dynamic response, steady-state error in the load voltage, controller complexity, robustness, and switching frequency. A detailed comparison of different DVR topologies and control strategies is presented in [22]. The common component of the DVR topologies mentioned so far is the series transformer used to inject the compensating voltage into the grid. Although the series transformer provides an electrical isolation between the PCC and DVR, it makes the DVR to be bulky and costly which is not suitable for office and home environments. Furthermore, it may enter into the saturation due to the magnetization phenomenon. Despite the saturation is prevented in [23], the use of series transformer still results in a bulky and costly DVR device.

Hence, there is a tendency to design transformerless DVR (TDVR) topologies [24]–[26] as well as universal active power filters [27]–[29] and operate them so as to achieve the required objectives without requiring a bulky and costly series injection transformer. In the case of TDVR, the filter capacitor of the TDVR is connected in series between the grid and load. Therefore, the objective of TDVR is to control the voltage across the series-connected capacitor such that the load voltage is not af-

Manuscript received June 4, 2016; revised September 13, 2016 and October 13, 2016; accepted November 8, 2016. Date of publication December 7, 2016; date of current version March 8, 2017.

H. Komurcugil is with the Computer Engineering Department, Eastern Mediterranean University, Mersin 10, Turkey (e-mail: hasan.komurcugil@emu.edu.tr).

S. Biricik is with the Department of Electrical and Electronic Engineering, European University of Lefke, Mersin 10, Turkey, and also with the School of Electrical and Electronic Engineering, Dublin Institute of Technology, Dublin 2, Ireland (e-mail: samet@biricikelektrik.com).

Color versions of one or more of the figures in this paper are available online at http://ieeexplore.ieee.org.

Digital Object Identifier 10.1109/TIE.2016.2636806

fected from the voltage variations in the grid. In [24] and [25], the capacitor voltage is controlled by employing H-bridge VSI. Recently, Kumar and Mishra [26] proposed a TDVR employing a half-bridge VSI which is controlled using a predictive control approach to achieve the capacitor voltage control. Although the presented results are satisfactory, the prediction of the reference capacitor voltage is essential and dependent on the filter parameters. Therefore, the performance of the predictive control is subject to degradation when the reference capacitor voltage prediction is not accurate due to the variations in the filter parameters.

The sliding-mode control (SMC) offers significant advantages like fast dynamic response, strong robustness to the parameter variations, and simplicity in the practical implementation. The SMC strategy with these advantages is applied to the control of DVRs [11]–[15]. In [11], the sliding surface function is formed by using capacitor voltage and inductor current errors in which the measurements of inductor current and capacitor voltage are required. In addition, the computation of the sliding surface function requires two coefficients which increase the implementation complexity. In [12] and [13], the computation of the sliding surface function is based on the capacitor voltage error and its derivative using only one coefficient. Recently, an SMC method with maximized existence region is proposed for single-phase DVR which employs an injection transformer [15]. Although the existence region is maximized by selecting the optimum sliding coefficient, the switching frequency is still time varying.

In this paper, time-varying and constant switching frequency-based SMC methods are presented for three-phase TDVRs employing half-bridge VSI. The existence conditions of the sliding-mode are determined. In addition, the time-varying switching frequency equation is derived analytically which can be used to predict the switching frequency. However, since the time-varying switching frequency is not desired in practice, a smoothing operation is applied to the sliding surface function within a narrow boundary layer with the aim of eliminating the chattering effect and achieving a constant switching frequency operation. The pulse width modulation (PWM) signals of the switching devices are generated by comparing the control signal obtained from the smoothing operation with a triangular carrier signal. The theoretical considerations and feasibility of both SMC methods are validated by the experimental results under distorted grid voltage and voltage sag conditions.

II. Mathematical Model of Three-Phase TDVR

Fig. 1 shows the block diagram of a three-phase TDVR with the proposed SMC methods. Each phase of TDVR consists of a half-bridge VSI, a coupling inductor L_f, and a series-connected capacitor $C_{\rm se}$. The output terminals of the half-bridge VSI are connected across $C_{\rm se}$ so as to inject a compensation voltage when needed. The operation of the system can be described by the following equations:

$$L_f \frac{di_{\rm fk}}{dt} = u_k V_{\rm dc} + v_{{\rm se},k} \tag{1}$$

$$C_{\rm se} \frac{dv_{{\rm se},k}}{dt} = -i_{\rm sk} - i_{\rm fk} \tag{2}$$

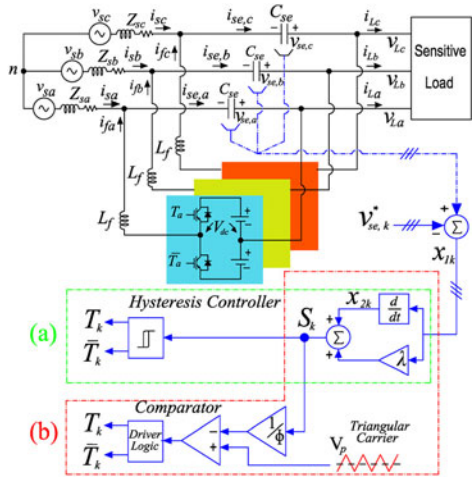

Fig. 1. Block diagram of three-phase TDVR with the proposed SMC methods. (a) Time-varying switching frequency based SMC method. (b) Constant switching frequency-based SMC method.

where u_k denotes the control input defined as

$$u_k = \begin{cases} 1 & T_k \text{ on} \\ -1 & \bar{T}_k \text{ on} \end{cases}, k = a, b, c. \tag{3}$$

The switching of T_k and $\bar{T}_k$ should be done in such a way that a compensation voltage is produced across $C_{\rm se}$ with the aim of keeping the load voltage sinusoidal and at a desired level for all times during the voltage distortions and sags occurring in the grid voltage.

III. SMC and Its Existence Condition

Let us define the state variables as

$$x_{1k} = v_{{\rm se},k} - v^*_{{\rm se},k} \tag{4}$$

$$x_{2k} = \dot{x}_{1k} = \dot{v}_{{\rm se},k} - \dot{v}^*_{{\rm se},k} \tag{5}$$

where $v^*_{{\rm se},k}$ is the reference for $v_{{\rm se},k}$. The sliding surface function and its derivative can be defined as

$$S_k = \lambda x_{1k} + x_{2k} \tag{6}$$

$$\dot{S}_k = \lambda \dot{x}_{1k} + \dot{x}_{2k} \tag{7}$$

where λ denotes the positive sliding coefficient. Taking the derivative of (5) and substituting (2) into the resulting equation yields

$$\dot{x}_{2k} = -\frac{1}{C_{\rm se}} \frac{di_{\rm sk}}{dt} - \frac{1}{C_{\rm se}} \frac{di_{\rm fk}}{dt} - \frac{d^2 v^*_{{\rm se},k}}{dt^2}. \tag{8}$$

Substitution of (1) in (8) gives

$$\dot{x}_{2k} = -\frac{1}{C_{\rm se}} \frac{di_{\rm sk}}{dt} - \frac{1}{L_f C_{\rm se}} (v_{{\rm se},k} + u_k V_{\rm dc}) - \frac{d^2 v^*_{{\rm se},k}}{dt^2}. \tag{9}$$

Now, substituting $v_{{\rm se},k} = x_{1k} + v^*_{{\rm se},k}$ in (9) and rearranging results in

$$\dot{x}_{2k} = -\omega_o^2 (x_{1k} + u_k V_{\rm dc}) - \omega_o^2 D_k(t) \tag{10}$$

where $\omega_o^2 = 1/L_f C_{\rm se}$ and $D_k(t)$ denotes the disturbance given by

$$D_k(t) = -L_f \frac{di_{\rm sk}}{dt} - L_f C_{\rm se} \frac{d^2 v^*_{{\rm se},k}}{dt^2} + v^*_{{\rm se},k}. \quad (11)$$

Substitution of (8) in (7) results in

$$\dot{S}_k = \lambda x_{2k} - \omega_o^2 (x_{1k} + u_k V_{\rm dc}) - \omega_o^2 D_k(t). \quad (12)$$

Let the control input described in (3) be generated by

$$u_k = \text{sign}(S_k). \quad (13)$$

In the sliding-mode, the state trajectory should be maintained on $S_k = 0$ by making a zigzag motion. As pointed out in [13], [15], [30]–[32], such motion (see Fig. 3) can be easily obtained by (13). It is obvious from (6) and (13) that the SMC does not depend on system parameters implying that the SMC is robust against parameter variations.

In designing a sliding-mode controller, the assurance of the existence condition during the sliding-mode operation is essential. The existence of the sliding-mode can be assured if S_k and $\dot{S}_k$ have the opposite signs satisfying the following condition [30]:

$$S_k \dot{S}_k < 0. \quad (14)$$

The existence condition of the sliding-mode for each switching device can be obtained as the following.

When $\bar{T}_k$ is turned ON,

$$S_k < 0 \Rightarrow \; u_k = -1 \quad (15)$$

$$\dot{S}_k > 0 \Rightarrow \; l_{1k} = \dot{S}_k = -\omega_o^2 x_{1k} + \lambda x_{2k} + d_{1k}(t) > 0\,. \quad (16)$$

When T_k is turned ON,

$$S_k > 0 \Rightarrow \; u_k = 1 \quad (17)$$

$$\dot{S}_k < 0 \Rightarrow \; l_{2k} = \dot{S}_k = -\omega_o^2 x_{1k} + \lambda x_{2k} + d_{2k}(t) < 0. \quad (18)$$

In (16) and (18), $d_{1k}(t)$ and $d_{2k}(t)$ are defined as

$$d_{1k}(t) = \; \omega_o^2 \left[V_{\rm dc} - D_k(t)\right] \quad (19)$$

$$d_{1k}(t) = \; -\omega_o^2 \left[V_{\rm dc} + D_k(t)\right]. \quad (20)$$

The existence area of the sliding-mode is bounded by lines l_{1k} and l_{2k}. When the sliding-mode exists, the sliding surface function is enforced to slide toward the origin ($x_{1k} = x_{2k} = 0$) along the sliding line ($S_k = 0$). Therefore, the sliding surface function and its derivative are both zero during the sliding-mode ($S_k = 0$, $\dot{S}_k = 0$). Hence, in the sliding-mode, (7) can be written as

$$\ddot{x}_{1k} + \lambda \dot{x}_{1k} = 0. \quad (21)$$

The solution of the above differential equation can easily be obtained as

$$x_{1k}(t) = x_{1k}(0) e^{-\lambda t} \quad (22)$$

where $-\lambda$ is the pole of the sliding-mode dynamics. It is evident from (22) that $x_{1k}(t)$ converges to zero if the sliding coefficient is selected as $\lambda > 0$. With $x_{1k}(t) = 0$, it follows from (5) that x_{2k} converges to zero as well. It is worth to note that the TDVR injects $v_{{\rm se},k}$ in the case of grid voltage anomalies. In the absence of these voltage anomalies in the grid ($v_{\rm Lk} = v_{\rm sk}$), both state variables are zero since the actual and desired capacitor voltages are zero ($v^*_{{\rm se},k} = v^*_{\rm Lk} - v_{\rm sk} = 0$). Since $x_{1k}(t) \to 0$ and $x_{2k} \to 0$ in the sliding-mode, it can be concluded that the stability of the system is guaranteed during the voltage anomalies existing in the grid. Fig. 2 shows the stability area in the phase plane (x_{1k} , x_{2k} plane). It is important to note that the sliding-mode occurs if the trajectory hits the sliding line between the points S_{1k} and S_{2k}. When the voltage sag occurs in the grid, x_{1k} becomes negative as shown in the third quadrant of Fig. 2. Thereafter, the trajectory is directed toward the line $S_k = 0$. When it hits $S_k = 0$, the proposed control starts to govern the movement of the trajectory. As mentioned before, the sliding-mode is known to be insensitive to parameter variations. This fact can be clearly seen from (22).

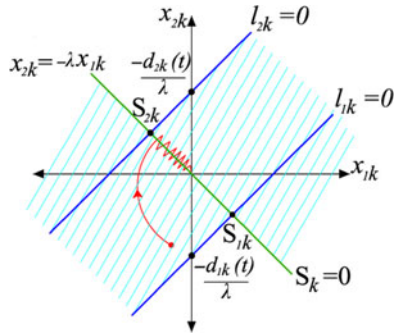

Fig. 2. Stability area in the phase plane.

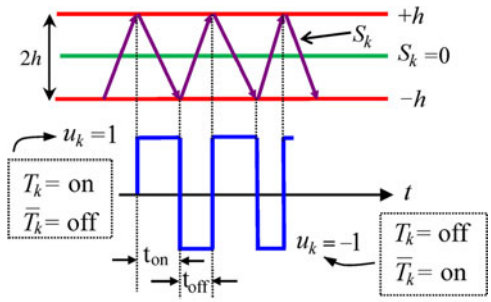

Fig. 3. Evolution of S_k and switching logic.

It should be noted that the implementation of the control input described in (13) results in a very high switching frequency which in turn causes undesired chattering. Therefore, the switching frequency is controlled and chattering is reduced by employing a hysteresis control consisting of a boundary layer as follows:

$$u_k = \begin{cases} 1 \;\; , \; S_k > +h \\ -1 \; , \; S_k < -h \end{cases}. \quad (23)$$

Evolution of the sliding surface function and switching logic are shown in Fig. 3. The sliding surface function is forced to slide along $S_k = 0$ within lower $(-h)$ and upper $(+h)$boundaries.

When S_k goes below $-h$, $\bar{T}_k$ is turned ON and $-V_{\rm dc}$ is applied to the $L_f C_{\rm se}$ filter. On the other hand, when S_k goes above $+h$, T_k is turned ON and $+V_{\rm dc}$ is applied to the filter.

IV. SMC With Time-Varying and Constant Switching Frequency

A. Time-Varying Switching Frequency-Based SMC

The switching frequency expression in terms of hysteresis band and other parameters plays an important role in the realization of the control method in real time. Here, the switching frequency derivation is done for T_a and $\bar{T}_a$. Assuming that the state variables are negligibly small ($x_{1a} = x_{2a} = 0$) in the steady state, (12) can be written as

$$\dot{S}_a \cong -\omega_o^2 \left[u_a V_{\rm dc} + D_a(t)\right]. \tag{24}$$

The reference voltage for the series-connected capacitor can be written as

$$v^*_{{\rm se},a} = V_{\rm La}\sin(\omega t) - V_{\rm sa}\sin(\omega t) = V_{\rm se}\sin(\omega t). \tag{25}$$

The second derivative of (25) with respect to time is obtained as

$$\frac{d^2 v^*_{{\rm se},a}}{dt^2} = -\omega^2 V_{\rm se}\sin(\omega t). \tag{26}$$

Assume that the load draws the following sinusoidal current from the grid

$$i_{\rm sa} = i_{\rm La} = I_s \sin(\omega t - \theta). \tag{27}$$

Taking the derivative of (27) yields

$$\frac{di_{\rm sa}}{dt} = \omega I_s \cos(\omega t - \theta). \tag{28}$$

Now, substituting (25), (26), and (28) into (11) results in

$$D_a(t) = K\cos(\omega t - \varphi) \tag{29}$$

where

$$K = \sqrt{K_1^2 + K_2^2 + 2K_1K_2\sin(\theta)} \tag{30}$$

$$K_1 = -V_{\rm se}\left((\omega_o^2 + \omega^2)/\omega_o^2\right) \tag{31}$$

$$K_2 = \omega L_f I_s \tag{32}$$

$$\varphi = \tan^{-1}\left((K_1 + K_2\sin(\theta))/K_2\right). \tag{33}$$

Substituting (29) into (24), we obtain

$$\dot{S}_a \cong -\omega_o^2 \left[u_a V_{\rm dc} + K\cos(\omega t - \varphi)\right]. \tag{34}$$

It is worth to note that for the values used in the simulation and experimental studies, the phase shift can be approximated as $\varphi \cong -90^\circ$. This implies that $K\cos(\omega t + 90^\circ) = -K\sin(\omega t)$ and

$$\dot{S}_a \cong -\omega_o^2 \left[u_a V_{\rm dc} - K\sin(\omega t)\right]. \tag{35}$$

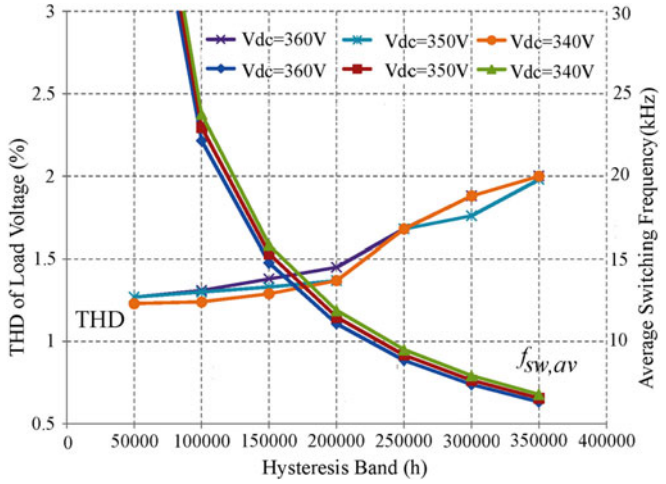

Fig. 4. Effect of changing h on the THD and $f_{\rm sw,av}$ with different $V_{\rm dc}$ values.

The ON and OFF durations of T_a and $\bar{T}_a$ can be formulated as

$$t_{\rm on} = \frac{-2h}{\dot{S}\,|_{u=1}} = \frac{2h}{\omega_o^2\left[V_{\rm dc} - K\sin(\omega t)\right]} \tag{36}$$

$$t_{\rm off} = \frac{2h}{\dot{S}\,|_{u=-1}} = \frac{2h}{\omega_o^2\left[V_{\rm dc} + K\sin(\omega t)\right]}. \tag{37}$$

Now, the switching frequency equation can be obtained as

$$f_{\rm sw} = \frac{1}{t_{\rm on} + t_{\rm off}} = \frac{\omega_o^2 V_{\rm dc}}{4h} - \frac{\omega_o^2 K^2}{4hV_{\rm dc}}\sin^2(\omega t). \tag{38}$$

It is evident from (38) that the switching frequency is time varying and dependent on the filter parameters, hysteresis band, and dc input voltage. Although the switching frequency can be controlled by the hysteresis band, the effect of chattering is not completely eliminated and the time-varying switching frequency still exists. The average switching frequency can be obtained by integrating (38) as follows:

$$f_{\rm sw,av} = \frac{1}{\pi}\int_0^\pi f_{\rm sw}\, d\omega t = \frac{\omega_o^2}{8hV_{\rm dc}}(2V_{\rm dc}^2 - K^2). \tag{39}$$

Targeted $f_{\rm sw,av}$ can be achieved by selecting the appropriate values of $V_{\rm dc}$, h, L_f, and $C_{\rm se}$. For a fixed $V_{\rm dc}$ value, increasing h would result in smaller $f_{\rm sw,av}$ and vice versa. However, the effect of changing h (for the sake of obtaining the targeted switching frequency) on the THD of load voltage should be investigated. Using the parameters provided in Section V, various simulations have been carried out using MATLAB/Simulink. The results are shown in Fig. 4. It is evident that h and $V_{\rm dc}$ are to be selected to make a compromise between the THD load voltage and average switching frequency.

B. Constant Switching Frequency-Based SMC

An alternative way to eliminate the chattering effect and achieve a constant switching frequency is to employ a PWM instead of the hysteresis modulation. The PWM is based on comparing the desired control signal with a triangular carrier signal.

The comparison process produces an output signal whose frequency is equal to the frequency of the carrier signal. The desired control signal is obtained from a smoothing operation applied to the control discontinuity within a narrow boundary layer introduced in the vicinity of the sliding surface function [30]. It is worth to note that the smoothing operation is performed to eliminate the chattering. All trajectories starting inside the boundary layer should be maintained inside the boundary layer. On the other hand, the trajectories starting outside the boundary layer are directed toward the boundary layer.

In order to achieve these requirements, the sliding surface function is interpolated inside the boundary layer with a thickness Φ by replacing the discontinuous control in (13) by S_k/Φ. However, as mentioned in [30], the result of smoothing does not guarantee a perfect tracking and, therefore, Φ is to be selected to make a compromise between tracking error and smoothing operation. Replacing S_k by S_k/Φ gives

$$\frac{S_k}{\Phi} = \frac{\lambda x_{1k} + x_{2k}}{\Phi} = \frac{\lambda x_{1k}}{\Phi} + \frac{1}{\Phi C_{\rm se}}(i_{{\rm se},k} - i^*_{{\rm se},k}). \quad (40)$$

The capacitor current error can be written as

$$i_{{\rm se},k} - i^*_{\rm se,k} = -(i_{\rm fk} + i_{\rm Lk}) - C_{\rm se}\frac{dv^*_{{\rm se},k}}{dt}. \quad (41)$$

Substituting $i_{\rm Lk} = (\Delta v_{\rm Lk} + v^*_{\rm Lk})/R_L$ in (41) for a resistive load of R_L gives

$$i_{{\rm se},k} - i^*_{{\rm se},k} = -(i_{\rm fk} - i^*_{\rm fk}) - (\Delta v_{\rm Lk}/R_L) \quad (42)$$

where $\Delta v_{\rm Lk} = v_{\rm Lk} - v^*_{\rm Lk}$. Since the main objective of TDVR is to maintain the load voltage at the desired level, then the load voltage error can be considered zero for all times ($\Delta v_{\rm Lk} = 0$). Now, substitution of (42) with $\Delta v_{\rm Lk}$ set to zero into (38) results in

$$\frac{S_k}{\Phi} = \frac{\lambda x_{1k}}{\Phi} - \frac{1}{\Phi C_{\rm se}}(i_{\rm fk} - i^*_{\rm fk}). \quad (43)$$

The λx_{1k} term in (43) denotes the multiplication of capacitor voltage error with the slope of the sliding line [31]. Since the inductor current ripple is much greater than the capacitor voltage ripple, then (43) can be approximated as

$$\frac{S_k}{\Phi} \cong \frac{-1}{\Phi C_{\rm se}}(i_{\rm fk} - i^*_{\rm fk}). \quad (44)$$

In [32], the slope of (44) is defined as

$${\rm Slope}_{S_k/\Phi} = V_{\rm dc}/(4L_f C_{\rm se}\Phi). \quad (45)$$

On the other hand, the slope of a triangular carrier can be expressed as [33]

$${\rm Slope}_{\rm carrier} = 4V_p f_{\rm sw} \quad (46)$$

where V_p and $f_{\rm sw}$ denote the amplitude and frequency of the carrier signal, respectively. It is well known that the PWM generation process can work properly if the following condition holds:

$${\rm Slope}_{S_k/\Phi} = (V_{\rm dc}/(4L_f C_{\rm se}\Phi)) < 4V_p f_{\rm sw} = {\rm Slope}_{\rm carrier}. \quad (47)$$

Hence, the lower bound of Φ is determined from

$$(V_{\rm dc}/(16L_f C_{\rm se} V_p f_{\rm sw})) < \Phi. \quad (48)$$

In order to achieve a proper smoothing process, the value of Φ should be determined precisely. With $\dot{S}_k/\Phi$, following the same approach applied in the derivation of (15)–(20), the same stability area shown in Fig. 2 can be obtained.

V. Simulation and Experimental Verification

The performances of both SMC methods have been verified with experiments performed by using OPAL-RT real-time platform and its associated tools [34]. The OPAL-RT controls the interactions between the console PC, CPUs, and field programmable gate array (FPGA) architecture. Hardware implementation of the proposed power system was achieved with an FPGA architecture which was developed using the Xilinx system generator tool. Block diagram of the three-phase TDVR with the proposed SMC methods is shown in Fig. 1. In the experimental tests, which are obtained by using the system parameters $V_{\rm dc} = 350$ V, $L_f = 0.6867$ mH, $C_{se} = 50$ μF, $V_g = 230\sqrt{2}$ V, RL load $= 54.16\ \Omega + 50$ mH, $\lambda = 5397$, $h = 200\,000$, $\Phi = 282\,000$, and $V_p = 1$ V, the harmonic compensation and voltage sag compensation abilities of the proposed SMC methods are investigated.

A. Dynamic Harmonic Compensation Test

Fig. 5 shows experimental results obtained by the time-varying switching frequency-based SMC method under highly distorted grid voltages. The total harmonic distortion (THD) of grid voltages is 12.38% as shown in Fig. 5(a). Also, the three-phase grid voltages are unbalanced such that phase to neutral voltages for each phase are 240.4, 226.3, 247.5 V, respectively. This means that the grid voltages are not only distorted, but are also unbalanced. It is evident from Fig. 5(b) that the TDVR injects the necessary compensation voltages $(v_{{\rm se},k})$ for each phase during the distortions and unbalances occurring in the grid with the aim of compensating the harmonic voltage distortions and achieving balanced three-phase voltages on the load terminals. Clearly, when there is no distortion in the grid, the TDVR does not attempt to inject any voltage to the grid. Despite the highly distorted and unbalanced grid voltages, the TDVR with the proposed time-varying switching frequency-based SMC is quite successful in maintaining the desired sinusoidal voltages on the load terminals as can be seen in Fig. 5(c). The THD of the voltage is reduced from 12.38% to 1.83%.

Fig. 6 shows the experimentally obtained results using the constant switching frequency-based SMC method under the same grid voltage conditions mentioned in Fig. 5. The switching frequency is set to 12.5 kHz. It is obvious from Fig. 6(b) that the TDVR injects the required compensation voltages for each phase avoiding the occurrence of harmonics and unbalance on the load terminals. It is evident from Fig. 6(c) that the load voltages are three-phase-balanced sinusoidal waveforms which are almost not affected from the variations in the grid. The THD of the load voltage is reduced from 12.38% to 1.33%.

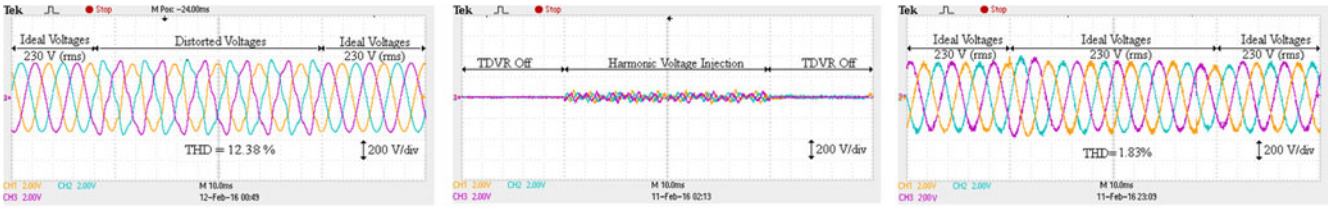

Fig. 5. Experimental responses of v_{sk}, $v_{\mathrm{se},k}$, and v_{Lk} obtained by the time-varying switching frequency-based SMC under distorted grid voltages. (a)v_{sk}, (b) $v_{\mathrm{se},k}$, and (c) v_{Lk}.

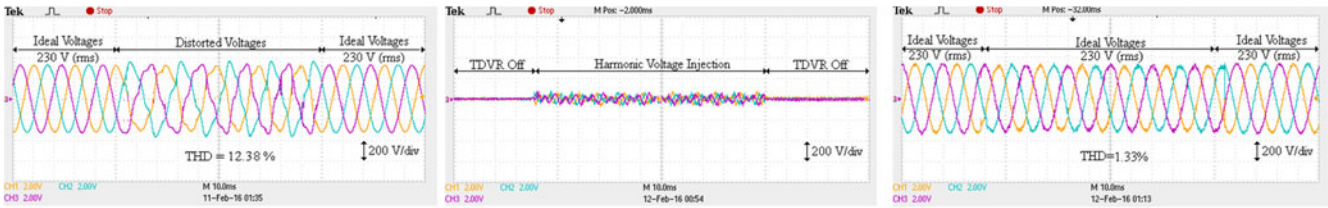

Fig. 6. Experimental responses of v_{sk}, $v_{\mathrm{se},k}$, and v_{Lk} obtained by the constant switching frequency-based SMC under distorted grid voltages. (a)v_{sk}, (b) $v_{\mathrm{se},k}$, and (c) v_{Lk}.

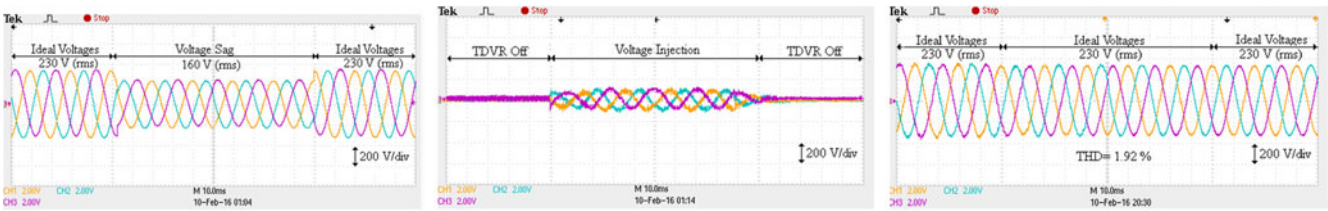

Fig. 7. Experimental responses of v_{sk}, $v_{\mathrm{se},k}$, and v_{Lk} obtained by the time-varying switching frequency-based SMC under voltage sags. (a)v_{sk}, (b) $v_{\mathrm{se},k}$ and (c) v_{Lk}.

Comparing the THDs of load voltages obtained by both SMC methods under a distorted and unbalanced grid voltage condition, one can easily see that the THD for constant switching frequency-based SMC is smaller than that of time-varying-based SMC. The main contribution of this THD improvement comes from the constant switching frequency operation of the VSI. It is worth to note that in the case of time-varying switching frequency-based SMC, the frequency varies between 10.5 and 14.5 kHz (see Fig. 9) which makes the THD of load voltage larger compared with the constant switching frequency operation.

B. Dynamic Voltage Sag Compensation Test

In this section, the performance of both SMC methods are investigated under voltage sags occurring in the grid. The amount of voltage sag is considered to be 70 V (rms). Fig. 7 shows the experimental responses of grid, injected, and load voltages obtained by the time-varying switching frequency-based SMC method when voltage sags exist in all phases in the grid. Fig. 7(a) shows the response of grid voltages under the voltage sags from 230 (rms) to 160 V (rms) and back to 230 V (rms). The performance of the controller for these sags can be seen in Fig. 7(b) and (c). Clearly, the TDVR with the proposed control method injects the required compensation voltages to compensate the voltage sags and maintain the load voltages at the desired level. Note that when there is no voltage sag, the TDVR does not inject any voltage. It is evident from Fig. 7(c) that the load voltage waveforms are balanced and undistorted. The THD of the load voltage is measured to be 1.92%.

The experimental performance of the constant switching frequency-based SMC system is also tested under the same voltage sag condition presented in Fig. 7. The results are depicted in Fig. 8. Clearly, the TDVR injects the required compensation voltages as shown in Fig. 8(b). As a consequence of the injected compensation voltages, the load voltages are almost not affected from the voltage sags and are maintained to be sinusoidal, balanced, and undistorted as can be seen in Fig. 8(c). The THD of load voltage is measured to be 1.34%. Comparing the THDs of load voltages obtained by both SMC methods under this voltage sag condition, the constant switching frequency-based SMC is seen to lead to smaller THD than that of time-varying-based SMC.

Fig. 9 shows the experimental waveforms of the switching frequency for the switching devices (T_a and $\bar{T}_a$) on phase A leg of VSI and compensation voltage ($v_{\mathrm{se},a}$) that correspond

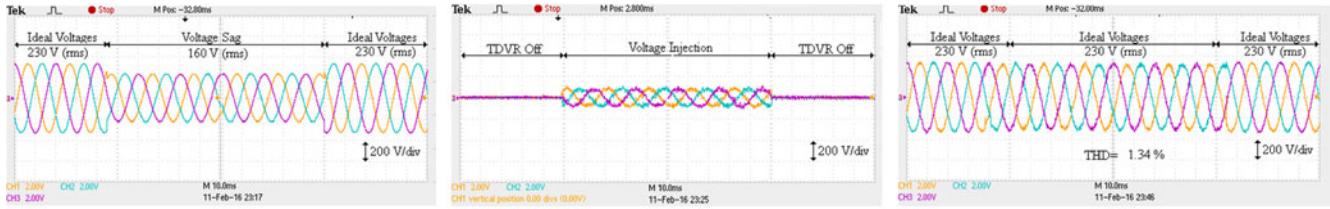

Fig. 8. Experimental responses of v_{sk}, $v_{\mathrm{se},k}$ and v_{Lk} obtained by the constant switching frequency-based SMC under voltage sags. (a)v_{sk}, (b) $v_{\mathrm{se},k}$, and (c) v_{Lk}.

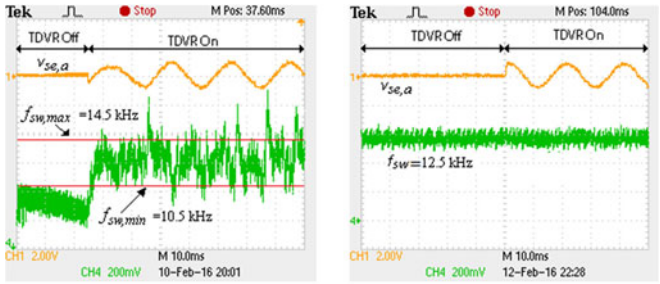

Fig. 9. Experimental waveforms of f_{sw} and $v_{\mathrm{se},a}$ under voltage sags. (a) f_{sw} and $v_{\mathrm{se},a}$ obtained by time-varying switching frequency-based SMC method, (b) f_{sw} and $v_{\mathrm{se},a}$ obtained by constant switching frequency-based SMC method.

to the voltage sag cases presented in Figs. 7 and 8. Fig. 9(a) shows the experimental waveforms of time-varying switching frequency together with the injected compensation voltage. It can be clearly seen that the switching frequency during the voltage injection period is time varying. It is worth to note that, in the experimental system, the switching frequency has been observed at the output of a monostable that is triggered by the gate signal of switching devices. Except the spikes occurring due to the noise in the gate signal of switching devices, the minimum and maximum switching frequencies were observed as 10.5 and 14.5 kHz, respectively. The minimum and maximum switching frequencies computed from (38) are 10.22 and 12.74 kHz, respectively. While computed and measured minimum switching frequencies agree well, there is a small discrepancy between computed and measured maximum frequencies due to the assumptions made in simplifying the theoretical derivation of the switching frequency. On the other hand, the sinusoidal behavior of the switching frequency at 100 Hz (see (38)) is not clearly visible in the experimental results due to the sampling time.

Fig. 9(b) shows the experimental waveforms of constant switching frequency together with the injected compensation voltage. It is clear that the switching frequency is always constant at 12.5 kHz before and during the voltage injection period.

C. Fault Ride-Through Capability

The amount of the voltage sags considered in Figs. 7 and 8 was approximately 30.43% of the grid voltage. In such a case, a short circuit current flows into a fault in the grid. The performance of the proposed SMC methods can also be investigated under worst grid faults such as single-phase to ground (asymmetrical) fault and three-phase to ground (symmetrical) fault. Fault ride-through (FRT) of the TDVR is the capability to restore and maintain the load voltage at the desired level in case of a fault occurs in the grid for a short period of time. However, due to the limited space, the FRT capability of the constant switching frequency-based SMC method is presented only. Fig. 10 shows the simulation results of grid, injected, and load voltages under a three-phase to ground fault in the grid at $t = 0.04$ s. It can be seen from Fig. 10(a) that the fault lasts two cycles. The TDVR injects the desired compensation voltages to clear the fault as shown in Fig. 10(b). As a consequence of this voltage injection, the load voltages are quickly restored after the fault [see Fig. 10(c)]. This indicates that the three-phase TDVR with the proposed constant switching frequency-based SMC method provides sufficient FRT behavior for a symmetrical fault existing in the grid.

Fig. 11 shows the simulation results of grid, injected, and load voltages under a single-phase to ground fault in the grid. It is evident that the TDVR compensates the faulted phase voltage quickly and restores the load voltage after the fault. These results clearly show that the TDVR operates efficiently to protect the loads under the asymmetrical and symmetrical faults existing in the grid.

D. Comparison With Existing Control Methods

The proposed SMC methods have considerably simpler structure compared with most of the existing control approaches. The TDVR with the proposed SMC methods and the DVR with the optimized SMC method proposed in [15] are modeled in Simulink using the same parameters given in [26]. These parameters are $V_{\mathrm{dc}} = 600$ V, $L_f = 10$ mH, $C_{\mathrm{se}} = 20\ \mu$F, $V_g = 230\sqrt{2}$ V, $f = 50$ Hz, $f_{\mathrm{sw,av}} = 4.2$ kHz, $\lambda = 2236$, and three-phase linear RL load ($60\ \Omega + 199.9$ mH, $40\ \Omega + 249.9$ mH, $50\ \Omega + 159.9$ mH). The hysteresis band was set to $h = 75000$ in order to have an average switching frequency of 4.2 kHz.

The simulation studies were carried out under linear RL load when 30% voltage sag exists in the grid. Fig. 12 shows the simulation results of v_{sk}, $v_{\mathrm{se},k}$, and v_{Lk} obtained by the SMC method presented in [15]. The THD of load voltage is computed to be 1.21%.

Figs. 13 and 14 show the simulation results of v_{sk}, $v_{\mathrm{se},k}$ and v_{Lk} obtained by the time-varying and constant switching frequency-based SMC methods, respectively. The THDs of load

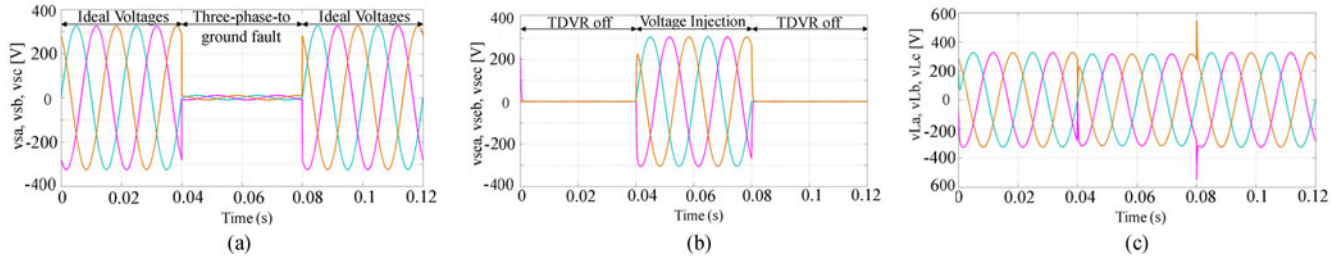

Fig. 10. Simulated responses of v_{sk}, $v_{\mathrm{se},k}$, and v_{Lk} obtained by the constant switching frequency-based SMC under three-phase-to-ground fault. (a)v_{sk}, (b) $v_{\mathrm{se},k}$, and (c) v_{Lk}.

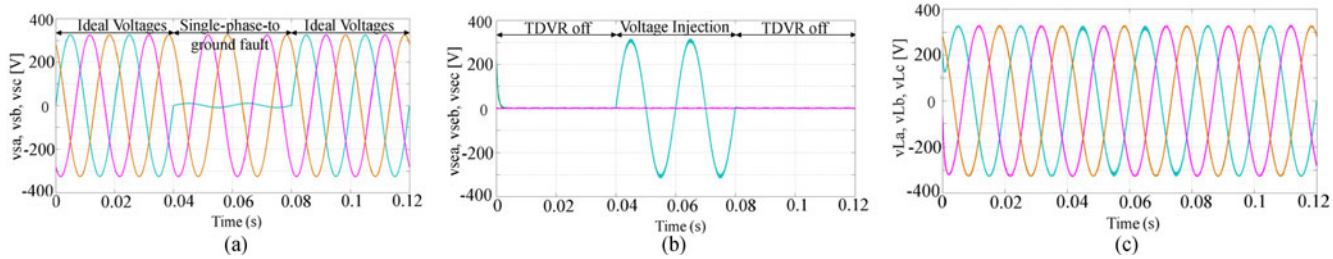

Fig. 11. Simulated responses of v_{sk}, $v_{\mathrm{se},k}$, and v_{Lk} obtained by the constant switching frequency-based SMC under single-phase-to-ground fault. (a)v_{sk}, (b) $v_{\mathrm{se},k}$, and (c) v_{Lk}.

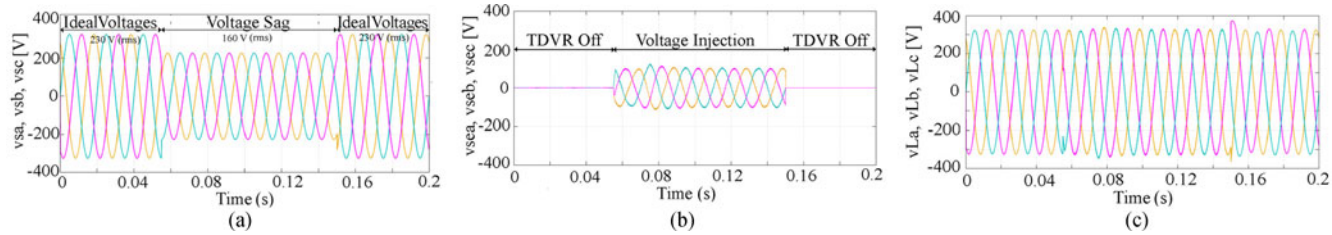

Fig. 12. Simulated responses of v_{sk}, $v_{\mathrm{se},k}$, and v_{Lk} obtained by the SMC method presented in [15]. (a)v_{sk}, (b) $v_{\mathrm{se},k}$, and (c) v_{Lk}.

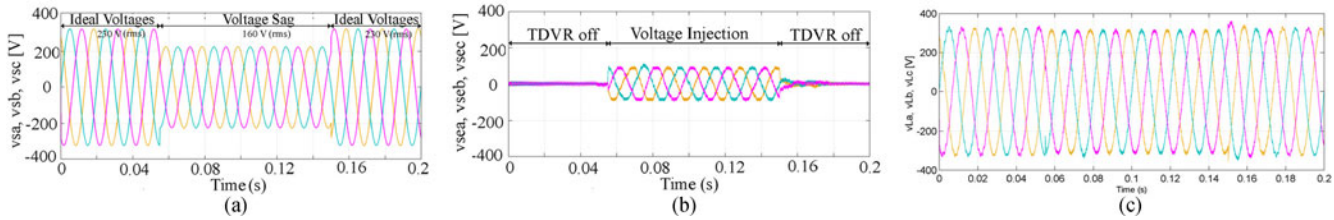

Fig. 13. Simulated responses of v_{sk}, $v_{\mathrm{se},k}$, and v_{Lk} obtained by the time-varying switching frequency-based SMC. (a)v_{sk}, (b)$v_{\mathrm{se},k}$, and (c) v_{Lk}.

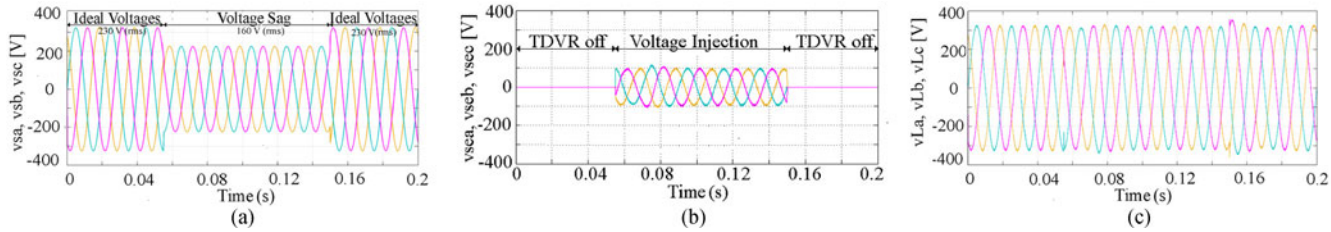

Fig. 14. Simulated responses of v_{sk}, $v_{\mathrm{se},k}$, and v_{Lk} obtained by the constant switching frequency-based SMC. (a)v_{sk}, (b) $v_{\mathrm{se},k}$, and (c) v_{Lk}.

TABLE I
COMPARISONS OF TWO CONTROL METHODS WITH THE PROPOSED SMC METHODS

Comparison	[15]	[26]	Proposed SMC Methods	
Category			Time-Var. f_{sw}	Constant f_{sw}
THD_{vL} (%)	1.21	1.20	0.91	0.80
Sensitivity to syst. param.	Insensitive	Sensitive	Insensitive	Insensitive
Size	Bulky with transformer	Smaller	Smaller	Smaller
Implementation complexity	Simple	Complex	Simple	Simple
Switching frequency	Variable	Fixed	Variable	Fixed
FRT capability	Not reported	Not reported	Reasonably fast	Reasonably fast

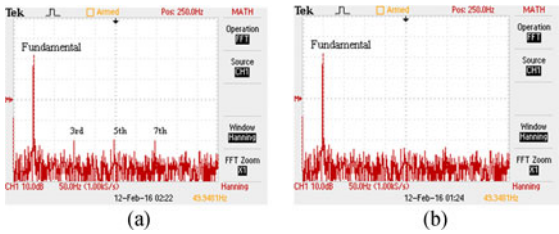

Fig. 15. Spectrums of load voltages that correspond to Figs. 7 and 8 obtained by: (a) time-varying switching frequency-based SMC, (b) constant switching frequency-based SMC.

voltages are computed as 0.91% and 0.8%, respectively. Comparing the results presented in Figs. 12–14 with the results presented in [26], one can see that the load voltages for the constant switching frequency-based SMC are less distorted than the others. These THD results together with the THD result in [26] are presented in Table I. Furthermore, the proposed SMC methods not only offers a significant advantage from the robustness point of view, but also leads to a relatively simpler implementation compared with the predictive voltage-based control method presented in [26].

Fig. 15 shows the load voltage spectrums obtained by time-varying and constant switching frequency-based SMC methods under the voltage sag condition presented in Figs. 7 and 8. Comparing the spectrums, the spectrum obtained by the time-varying switching frequency based SMC contains third, fifth, and seventh harmonics, while the spectrum obtained by the constant switching frequency-based SMC contains only the fundamental component. This means that the constant switching frequency-based SMC offers better quality load voltage. The main reason of this performance improvement comes from the fact that the load voltage distortion is minimized by the harmonics when the VSI is operated with the constant switching frequency.

VI. CONCLUSION

In this study, time-varying and constant switching frequency-based SMC methods were presented for three-phase TDVR employing half-bridge VSI. An analytical equation is derived to compute the time-varying switching frequency. Since, the time-varying switching frequency is not desired in a real application, a smoothing operation was applied to the sliding surface function within a narrow boundary layer with the aim of eliminating the chattering effect and achieving a constant switching frequency. The control signal obtained from the smoothing operation was compared with a triangular carrier signal to produce the PWM signals. It was observed that the smoothing operation results in a constant switching frequency operation at all times. The feasibility of both SMC methods has been validated by experimental results obtained from the TDVR operating under highly distorted grid voltages and voltage sags. The results obtained from both methods show excellent performance. However, the constant switching frequency-based SMC method not only offers a constant switching frequency at all times and preserves the inherent advantages of the SMC, but also leads to smaller THD in the load voltage than that of time-varying switching frequency-based SMC method.

REFERENCES

[1] M. Bollen, *Understanding Power Quality Problems*. New York, NY, USA: IEEE Press, 2000.
[2] B. Singh, A. Chandra, and K. Al-Haddad, *Power Quality Problems and Mitigation Techniques*. Chichester, U.K.: Wiley, 2015.
[3] Y. W. Li, F. Blaabjerg, D. M. Vilathgamuwa, and P. C. Loh, "Design and comparison of high performance stationary-frame controllers for DVR implementation," *IEEE Trans. Power Electron.*, vol. 22, no. 2, pp. 602–612, Mar. 2007.
[4] H. Kim and S. K. Sul, "Compensation voltage control in dynamic voltage restorers by use of feed forward and state feedback scheme," *IEEE Trans. Power Electron.*, vol. 20, no. 5, pp. 1169–1177, Sep. 2005.
[5] A. Khodabakhshian, M. Mahdianpoor, and R. A. Hooshmand, "Robust control design for multi-functional DVR implementation in distribution systems using quantitative feedback theory," *Elect. Power Syst. Res.*, vol. 97, pp. 116–125, 2013.
[6] Y. W. Li, F. Blaabjerg, D. M. Vilathgamuwa, and P. C. Loh, "Design and comparison of high performance stationary-frame controllers for DVR implementation," *IEEE Trans. Power Electron.*, vol. 22, no. 2, pp. 602–612, Mar. 2007.
[7] A. Teke, K. Bayindir, and M. Tümay, "Fast sag/swell detection method for fuzzy logic controlled dynamic voltage restorer," *IET Gener., Transmiss. Distrib.*, vol. 4, no. 1, pp. 1–12, 2009.
[8] P. R. Sanchez, E. Acha, J. E. O. Calderon, V. Feliu, and A. G. Cerrada, "A versatile control scheme for a dynamic voltage restorer for power-quality improvement," *IEEE Trans. Power Del.*, vol. 24, no. 1, pp. 277–284, Jan. 2009.
[9] S. Sasitharan and M. K. Mishra, "Constant switching frequency band controller for dynamic voltage restorer," *IET Power Electron.*, vol. 3, no. 5, pp. 657–667, 2010.
[10] P. Jayaprakash, B. Singh, D. P. Kothari, A. Chandra, and K. Al-Haddad, "Control of reduced-rating dynamic voltage restorer with a battery energy storage system," *IEEE Trans. Ind. Appl.*, vol. 50, no. 2, pp. 1295–1303, Mar./Apr. 2014.
[11] K. Piatek, "sliding-mode control of DVR with minimized energy injection," *Proc. Eur. Conf. Power Electron. Appl.*, 2005, pp. 1–8.
[12] R. R. Errabelli, Y. Y. Kolhatkar, and S. P. Das, "Experimental investigation of DVR with sliding-mode control," *Proc. IEEE Power India Conf.*, 2006.
[13] S. Biricik, H. Komurcugil, and M. Basu, "sliding-mode control strategy for three-phase DVR employing twelve-switch voltage source converter," in *Proc. 41st Annu. Conf. IEEE Ind. Electron. Soc.*, 2015, pp. 921–926.
[14] M. Mahalakshmi, S. Latha, and S. Ranjithpandi, "sliding-mode control for PMSG based dynamic voltage restorer," in *Proc. Int. Conf. Energy Efficient Technol. Sustain.*, 2013, pp. 1320–1323.
[15] S. Biricik and H. Komurcugil, "Optimized sliding-mode control to maximize existence region for single-phase dynamic voltage restorers," *IEEE Trans. Ind. Informat.*, vol. 12, no. 4, pp. 1486–1497, Aug. 2016.
[16] A. Ghosh, A. K. Jindal, and A. Joshi, "Design of a capacitor-supported dynamic voltage restorer (DVR) for unbalanced and distorted loads," *IEEE Trans. Power Del.*, vol. 19, no. 1, pp. 405–413, Jan. 2004.

[17] C. N. M. Ho, H. S. H. Chung, and K. T. K. Au, "Design and implementation of a fast dynamic control scheme for capacitor-supported dynamic voltage restorers," *IEEE Trans. Power Electron.*, vol. 23, no. 1, pp. 237–251, Jan. 2008.
[18] C. N. M. Ho and H. S. H. Chung, "Implementation and performance evaluation of a fast dynamic control scheme for capacitor-supported interline DVR," *IEEE Trans. Power Electron.*, vol. 25, no. 8, pp. 1975–1988, Aug. 2010.
[19] A. Elserougi, A. M. Massoud, A. S. Abdel-Khalik, S. Ahmed, and A. A. Hossam-Eldin, "An interline dynamic voltage restoring and displacement factor controlling device (IVDFC)," *IEEE Trans. Power Electron.*, vol. 29, no. 6, pp. 2737–2749, Jun. 2014.
[20] J. D. Barros and J. F. Silva, "Multilevel optimal predictive dynamic voltage restorer," *IEEE Trans. Ind. Electron.*, vol. 57, no. 8, pp. 2747–2760, Aug. 2010.
[21] E. Babaei, M. F. Kangarlu, and M. Sabahi, "Dynamic voltage restorer based on multilevel inverter with adjustable dc-link voltage," *IET Power Electron*., vol. 7, no. 3, pp. 576–590, 2014.
[22] J. G. Nielsen and F. Blaabjerg, "A detailed comparison of system topologies for dynamic voltage restorers," *IEEE Trans. Ind. Appl.*, vol. 41, no. 5, pp. 1272–1280, Sep./Oct. 2005.
[23] D. A. Fernandes, F. G. Costa, and M. A. Vitorino, "A method for averting saturation from series transformers of dynamic voltage restorers," *IEEE Trans. Power Del.*, vol. 29, no. 5, pp. 2239–2247, Oct. 2014.
[24] B. H. Li, S. S. Choi, and D. M. Vilathgamuwa, "Transformerless dynamic voltage restorer," *IEE Proc. Gener., Transmiss. Distrib.*, vol. 149, no. 3, pp. 263–273, May 2002.
[25] E. K. K. Sng, S. S. Choi, and D. M. Vilathgamuwa, "Analysis of series compensation and DC-link voltage controls of a transformerless self-charging dynamic voltage restorer," *IEEE Trans. Power Del.*, vol. 19, no. 3, pp. 1511–1518, Jul. 2004.
[26] C. Kumar and M. K. Mishra, "Predictive voltage control of transformerless dynamic voltage restorer," *IEEE Trans. Ind. Electron.*, vol. 62, no. 5, pp. 2693–2697, May 2015.
[27] W. R. N. Santos *et al.*, "The transformerless single-phase universal active power filter for harmonic and reactive power compensation," *IEEE Trans. Power Electron.*, vol. 29, no. 7, pp. 3563–3572, Jul. 2014.
[28] W. R. N. Santos, E. D. M. Fernandes, E. R. C. D. Silva, C. B. Jacobina, A. C. Oliveira, and P. M. Santos, "Transformerless single-phase universal active filter with UPS features and reduced number of electronic power switches," *IEEE Trans. Power Electron.*, vol. 31, no. 6, pp. 4111–4120, Jun. 2016.
[29] L. Limongi, L. da Silva Filho, L. Genu, F. Bradaschia, and M. Cavalcanti, "Transformerless hybrid power filter based on a six-switch two-leg inverter for improved harmonic compensation performance," *IEEE Trans. Ind. Electron.*, vol. 62, no. 1, pp. 40–51, Jan. 2015.
[30] J.-J. E. Slotine and W. Li, *Applied Nonlinear Control*. Englewood Cliffs, NJ, USA: Prentice-Hall, 1991.
[31] H. Komurcugil, "Rotating-sliding-line based sliding-mode control for single-phase UPS inverters," *IEEE Trans. Ind. Electron.*, vol. 59, no. 10, pp. 3719–3726, Oct. 2012.
[32] A. Abrishamifar, A. Ahmad, and M. Mohamadian, "Fixed switching frequency sliding-mode control for single-phase unipolar inverters," *IEEE Trans. Power Electron.*, vol. 27, no. 5, pp. 2507–2514, May 2012.
[33] N. R. Zargari, P. D. Ziogas, and G. Joos, "A two-switch high-performance current regulated DC/AC converter module," *IEEE Trans. Ind. Appl.*, vol. 31, no. 3, pp. 583–589, May/Jun. 1995.
[34] P. Kanjiya, B. Singh, A. Chandra, and K. Al-Haddad, "SRF theory revisited to control self-supported dynamic voltage restorer (DVR) for unbalanced and nonlinear loads," *IEEE Trans. Ind. Appl.*, vol. 49, no. 5, pp. 2330–2340, Sep./Oct. 2013.

Hasan Komurcugil (S'94–M'99–SM'12) received the B.Sc., M.Sc., and Ph.D. degrees in electrical and electronic engineering from the Eastern Mediterranean University (EMU), Mersin, Turkey, in 1989, 1991, and 1998, respectively.

In 1998, he joined the Computer Engineering Department, EMU, as an Assistant Professor, where he became an Associate Professor and a Professor in 2002 and 2008, respectively. From 2004 to 2010, he was the Head of the Computer Engineering Department, EMU. In 2010, he played an active role in preparing the department's first self-study report for the use of the Accreditation Board for Engineering and Technology. He is currently with the Computer Engineering Department, EMU, and a Board Member of the higher education, planning, evaluation, accreditation, and coordination council (YODAK) in North Cyprus. His research interests include power electronics and innovative control methods for power converters.

Prof. Komurcugil received Best Presentation Recognitions at the 41st and 42nd Annual Conferences of the IEEE Industrial Electronics Society in 2015 and 2016. He is a member of the Chamber of Electrical Engineers in North Cyprus. He is an Associate Editor of the IEEE TRANSACTIONS ON INDUSTRIAL INFORMATICS.

Samet Biricik (M'12) received the B.Sc. and Ph.D. degrees in electrical and electronic engineering from the Near East University, Mersin, Turkey, in 2006 and 2013, respectively.

From 2006 to 2016, he worked on various industrial and commercial projects. He is currently a Research Fellow in the School of Electrical and Electronic Engineering, Dublin Institute of Technology, Dublin, Ireland, and a Lecturer with the European University of Lefke, Lefke, Cyprus. His research interests include applications of power electronics, power quality, electrical machines, and high-voltage engineering.

Dr. Biricik received a Best Paper Award at the IEEE 9th International Conference on Environment and Electrical Engineering in 2010.